The unsteady wall shear stress vector of a high Reynolds number turbulent pipe flow obtained with multi-aperture defocusing microscopic particle tracking

J. Klinner[1,*], C. Willert[1], L. Magnani[2], A. Tallamelli[2], G. Bellani[2]

1: Institute of Propulsion Technology, German Aerospace Center (DLR), Köln, Germany
2: Department of Industrial Engineering / CIRI Aerospace, University of Bologna, Forlì, Italy
*Corresponding author: joachim.klinner@dlr.de

Keywords: fluid flow measurement, turbulent boundary layer, pipe flows, aperture encoding, particle tracking, PTV, depth-from-defocus

ABSTRACT

This study presents the first unsteady measurement of the wall shear stress (WSS) vector in a turbulent pipe flow up to $\mathrm{Re}_\tau = 28400$ using a single-camera, multi-aperture 3d-3c multi-aperture microscopic particle tracking velocimetry (MA-µPTV) system. By illuminating tracer particles from the side, the setup achieves higher scattering efficiency and reduces light scattering from window inclusions compared to backscattering configurations, doubling the number of successfully reconstructed particle triplets. This enables a spatial resolution of binaveraged statistics of $8\,\mu\mathrm{m}$ — approximately half the smallest viscous length scale — allowing direct access to the viscous sublayer and capturing near-wall turbulence with unprecedented fidelity. Velocity statistics up to the fourth moment are resolved at wall distances up to $600\,\mu\mathrm{m}$. The probability density functions (PDFs) and joint PDFs of the WSS and its rate of change exhibit strong Reynolds number independence, indicating self-similar near-wall dynamics governed by local viscous scaling. While streamwise WSS fluctuations follow expected scaling, the spanwise component $\tau_{z,\mathrm{rms}}$ remains significantly underestimated compared to flat plate turbulent boundary layer (TBL) correlations, even after extrapolation to $y^+ = 0$. In contrast, the spanwise component agrees with pipe flow direct numerical simulation (DNS) data within measurement uncertainty, likely due to geometric confinement and suppression of large-scale spanwise coherent structures compared to flat plate flow. These results contribute to establishing a new experimental benchmark for high-Reynolds-number wall-bounded turbulence.

Introduction

The CICLoPE facility (Centre for International Cooperation in Long Pipe Experiments), operated by the University of Bologna, is a unique research platform for studying turbulence in high-Reynolds-number flows. It enables the generation of flows with Reynolds numbers up to $Re_{\tau,\max} \approx 50\,000$, while maintaining access to viscous-scale resolution down to approximately $10\,\mu\mathrm{m}$. The facility features a 100-meter-long pipe with a diameter of $900\,\mathrm{mm}$, in which stable dynamic and thermal conditions can be sustained [14].

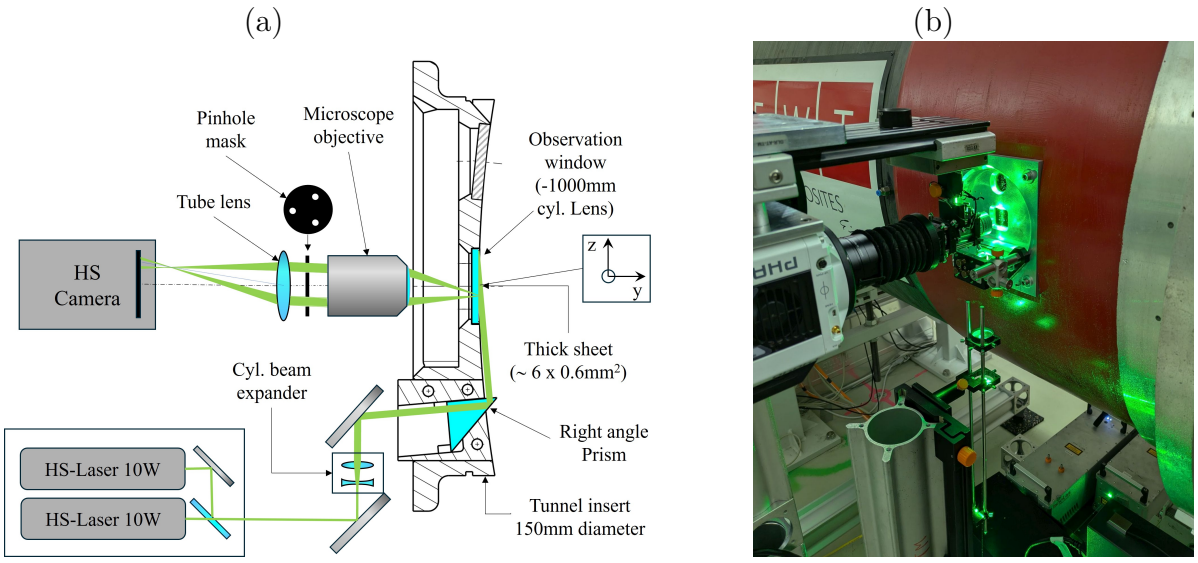

Figure 1. (a) Schematic of the MA-µPTV setup, (b) Photograph of the setup on the test section of the CICLoPE facilty.

The present contribution represents an effort to extend the MA-µPTV technique, recently validated for unsteady wall shear stress (WSS) measurements in a canonical planar TBL [6], to turbulent pipe boundary layers. The method enables three-dimensional particle tracking using a single camera, with the wall-normal distance of particles determined from the size of projected particle image triplets formed by a triplet of apertures at the entrance pupil of the microscope objective. This approach is based on the "defocusing" principle originally introduced by Willert & Gharib [15].

The present measurements build on experience gained from earlier high-speed profile PIV measurements conducted by the authors at CICLoPE [16]. In this setup, the previous tunnel insert was modified to include an additional access port, enabling side illumination of particles with a thick laser sheet for three-dimensional particle tracking.

To preserve the flow geometry in turbulent pipe flows, tracer particles must be observed through concave windows, requiring corrections for image distortion induced by the curvature. To this end, the calibration procedure for MA-µPTV has been modified and extended. While previous measurements in a canonical TBL employed a backscattering configuration [6], the present imaging setup uses side-scattering, which significantly increases light scattering efficiency and approximately doubles the number of particles per unit area. This enhancement improves spatial resolution and statistical convergence. On the other hand, it also imposes higher demands on the particle tracking algorithm, as the probability of incorrect particle matches increases accordingly.

Table 1. Acquisition parameters for near-wall turbulent pipe flow MA-µPTV measurements.

Centerline velocity [m/s]	$\mathbf{U}_{cl}$	**5.54**	**7.87**	**10.21**	**14.98**	**20.0**		**30.1**	
Reynolds number	Re_τ	5 940	8 200	10 400	14 900	19 400		28 400	
Friction velocity [m/s]	u_τ	0.201	0.277	0.352	0.502	0.657		0.962	
Viscous length scale [µm]	$l^* = \nu/u_\tau$	78.0	56.4	44.3	31.0	23.7		16.1	
Sampling rate [kHz]	f_{acq}	20	20	20	20	20	40	40	53
Number of sequences		16	16	32	32	32	32	32	32
Samples per sequence	N	14 096	14 096	7 038	7 038	5 550	14 076	14 076	18 736
Independent samples	N_{eff}	140	198	256	376	197	250	377	379
Magnification [µm pixel^{-1}]		1.8	1.8	1.8	1.8	1.8	3.6	3.6	3.6
Image Size [l^*]	$x^+ \times z^+$	47×18	65×25	83×31	119×45	194×58	155×117	228×171	228×128

Experimental Method

As outlined in Fig. 1(a), the high-speed camera (Vision Research T4040) and an infinity-corrected microscope lens (Mitotuyo Plan Apo 5×) image particles through a cylindrical window that matches the inner contour of the pipe ($R = 450\,\mathrm{mm}$). The objective is combined with a tube lens of $f = 180\,\mathrm{mm}$. In that way a field of view (FOV) of $3.7\,\mathrm{mm} \times 1.4\,\mathrm{mm}$ can be captured at an image size of 2048×768 pixel at a frame rate of $20\,\mathrm{kHz}$.

The pinhole mask consists of a black anodized aluminum foil and is placed in the nearly parallel optical path between the objective and the tube lens. The mask contains three precision-milled pinholes, each with $2\,\mathrm{mm}$ diameter, that form an equilateral triangle. The spacing between the pinholes is maximized such that the apertures are located within the entrance pupil diameter of the objective. The size of the triplet image of a particle projected through this triplet aperture varies linearly with the radial position of particles along y. The depth sensitivity of the microscopic setup is $89.3\,\mathrm{pixel/mm}$, which corresponds to an uncertainty in radial position of $\mathcal{O}(1\,\mathrm{\mu m})$ when assuming an uncertainty of $\mathcal{O}(0.1\,\mathrm{pixel})$ for the estimation of the triplet side length. The cylindrical window introduces an offset of the linear calibration that varies non-linearly across the field of view and was compensated for by a function consisting of a 2nd order polynomial along the streamwise (x) and circumferential or spanwise (z) axis.

A collimated laser sheet is provided by two high-speed pulsed lasers (2× Innolas Photonics Nanio Air) and introduced to the pipe by a right-angle prism, enabling grazing incidence on the window (see Fig. 1a). Both lasers have an average rated power of $10\,\mathrm{W}$ at a pulse repetition rate of $40\,\mathrm{kHz}$ and fire simultaneously, providing $\approx 0.5\,\mathrm{mJ}$ per pulse. Two cylindrical lenses expand the beam diameter to roughly $6\,\mathrm{mm} \times 0.6\,\mathrm{mm}$ along the streamwise (x) and radial (y) axis.

The flow is seeded with $d_p = [1-2]\,\mathrm{\mu m}$ long-lasting aerosol droplets from a water-based fog generator (HazeBase Classic, base*M fluid).

Table 1 provides an overview on test points for which sequences were acquired with MA-µPTV. Measurements were performed at centerline velocities of $U_{cl} = 5.5\,\mathrm{m/s}$ up to $30.1\,\mathrm{m/s}$ spanning

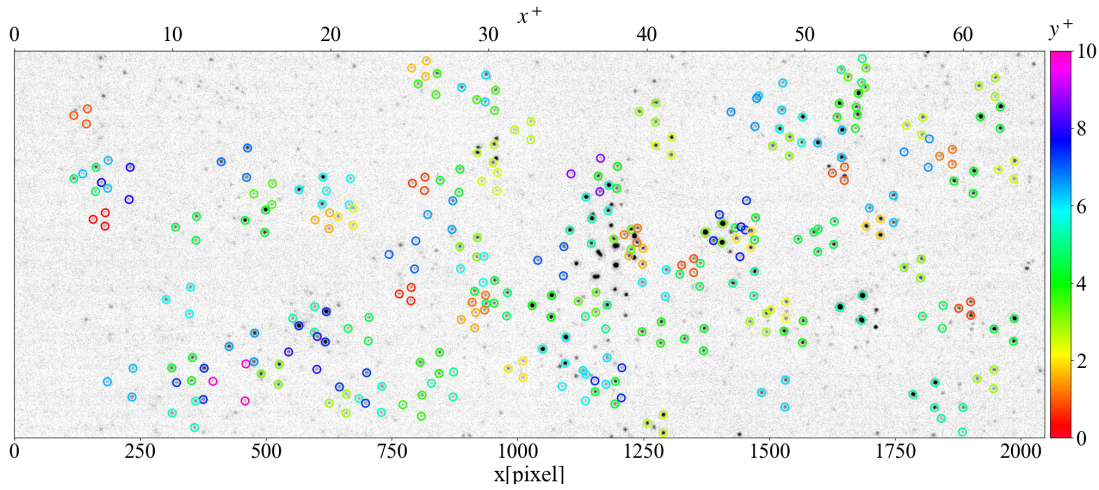

Figure 2. Processed MA-µPTV sample image at $U_{\mathrm{cl}} = 7.7\,\mathrm{m/s}$ ($\mathrm{Re}_\tau = 8\,200$) with detected triplets color-coded by the estimated wall distance.

a shear Reynolds number range of $\mathrm{Re}_\tau = 5\,900$ to $28\,400$. To match the mean flow velocity, the framing rate of the high-speed camera is varied between $20\,\mathrm{kHz}$ and $53\,\mathrm{kHz}$ with the former resulting in an image size of $2048\,\mathrm{pixel} \times 768\,\mathrm{pixel}$. At the highest two velocities 2×2 pixel binning was used to achieve the required high sampling rates resulting in images of $1024\,\mathrm{pixel} \times 768\,\mathrm{pixel}$ (Table 1 provides corresponding image sizes in viscous units). For each centerline velocity up to 32 sequences consisting of 7 000 to 18 100 images each constitute the basis for the subsequent 3d-PTV. The quantity N_{eff} indicates the number of independent samples in all sequences based on the eddy turnover time $\tau = R/U_{cl}$.

Image Processing and 3d-PTV

To minimize the artifacts introduced by window contamination by particle deposition, a sliding minimum over 20 frames is subtracted from each image. Next, particle images are first identified by template matching by convolving the image with a Gaussian template. Then a search is performed on the particle image centroids to find the vertices of triplet candidates. Matching is based on a similarity measure S of the triangle sides $\vec{a}_1$ to a reference vector $\vec{e}_1(x, y, z)$ that is determined by an a priori calibration procedure using a y-traversed mask of pinholes (see [6] for details).

Once a triplet is identified, the three particle image centers are refined using least-squares fitting of a 2d Gaussian with a predetermined width. The y position is calculated from the radius of the circumcircle of the triangle, using calibrated sensitivity. In contrast, the y position derived from the mean of the individual y_i values – based on the calibrated sensitivity of the side length $|\vec{a}_1|$, $|\vec{a}_2|$ – is less accurate. However, half of the maximum absolute deviation between the y_i-positions serves as measure of reconstruction quality. Fig. 2 shows a sample image at $U_{\mathrm{cl}} = 7.7\,\mathrm{m/s}$ with matched

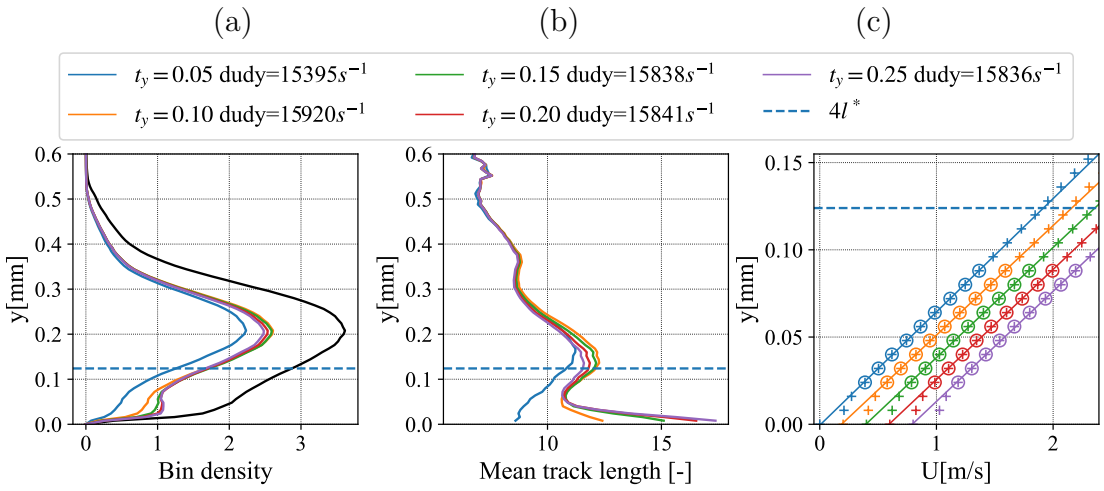

Figure 3. Bin densities (a) and mean track length (b) and Near-wall mean velocity profiles (c) at $U_{\mathrm{cl}} = 15\,\mathrm{m/s}$ ($\mathrm{Re}_\tau = 14900$) for a variation of t_y; The black curve in (a) shows the sum of tracked plus un-tracked particles; (c): u-offset $0.2\,\mathrm{m/s}$, + measured data, ∘ data included in fit, − linear fit to obtain the wall gradient.

triplets for which the maximum accepted disparity is $6\,\mu\mathrm{m}$.

Using the reconstructed particle positions, Lagrangian particle tracks were initialized with up to four image frames using classical techniques as described by [8, 10]. From candidates that are linked in four frames, the track with smallest change in velocity is selected (e.g. minimum acceleration criterion). To continue tracks beyond three members, the predicted displacement toward following frames is based on the velocity difference to the predecessor plus the displacement extrapolated from the acceleration in the previous two frames. For longer tracks, the predictor relies on a cubic polynomial fitted through the last four track members. A new element is assigned if it lies within the relative wall distance change t_y and its distance from the predictor is smaller than a circular search region with radius r_s. Following forward tracking across a sequence of frames, tracks with fewer than a specified number of members t_N are eliminated. With the spurious tracks removed, the entire tracking procedure is repeated for the remaining non-linked particles in backward time association, followed by removal of short tracks. To obtain the particle positions and velocity from the reconstructed track, least-squares regression is applied using a cubic B-spline fitting scheme. Weighting is applied at each vertex, using the disparity of each triplet. To get wall-normal profiles of various statistics (e.g. bin counts, velocities, WSS), a bin-averaging scheme was employed with a bin size of $8\,\mu\mathrm{m}$, which is smaller than half of the smallest viscous unit. The assignment into equally spaced bins is performed using bilinear weighting.

Fig. 3 shows example profiles of bin densities of tracked particles at $U_{\mathrm{cl}} = 15\,\mathrm{m/s}$ which were used for the optimization of the tracking parameters (e.g. t_y, t_N, r_s). In (a) the enclosing black curve indicates the overall bin density of tracked and un-tracked particles. The curve is affected by the laser power density, which reaches its maximum at $y = 0.2\,\mathrm{mm}$ and decreases with distance from the wall. For a variation of t_y, Fig. 3 shows that the bin counts and the mean track lengths in the

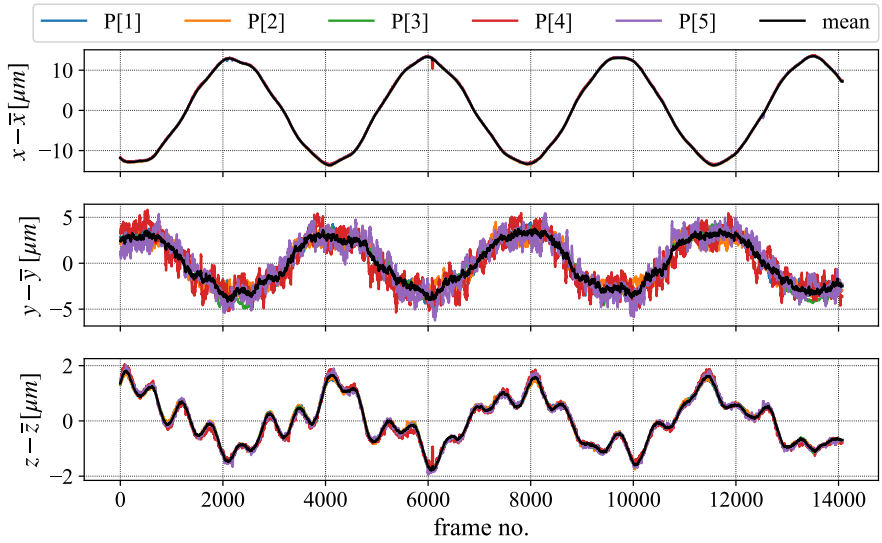

Figure 4. Vibrations of wall/camera position in an image sequence at U_{cl}=30.1 m/s obtained from five particles fixed to the wall.

viscous sublayer are largest at $t_y = 0.25$. However, it is assumed that correctly tracked particles maximize the wall gradient. Indeed, the velocity profile in (c) reveals a slight flattening of the wall gradient at $t_y = 0.25$ (wall gradients are provided in the plot legend) while the maximum gradient is achieved at $t_y = 0.1$, which also maximizes the track length within a wall distance range of $0.1\,\mathrm{mm} - 0.2\,\mathrm{mm}$. To capture additional tracks within the viscous sublayer, the previously described tracking procedure is repeated once on all un-tracked particles using a larger t_y. For $U_{\mathrm{cl}} = 15\,\mathrm{m/s}$, this results in a further increase in the gradient, yielding a friction velocity of $0.497\,\mathrm{m/s}$, which underestimates the pressure-based reference value by only 1% (see Table 1). For all measurements, the deviations between tracer-based and pressure-based estimates of u_τ ranged from $-2.8\,\%$ to $-0.15\,\%$. The observed underestimation is likely due to the particle's response dynamics.

Essential for the estimation of the wall shear stress is a precise knowledge of the wall position. This is achieved using a 2nd order polynomial fit of 3d positions of particles stuck to the curved inner surface of the viewing area. As the velocity increased, wall vibrations were observed; these were taken into account in the calculation of the wall shear stress by determining the transient wall position in each individual frame. Therefore, the offset was subtracted from the 3d particle positions in each frame prior to particle tracking. At $U_{cl} = 30\,\mathrm{m/s}$ Fig. 4 shows axial vibration amplitudes less then 1 viscous unit at $10.67\,\mathrm{Hz}$, which frequency corresponds to the fan's rotational speed. The WSS relevant wall-normal excursions are limited to $\pm 5\,\mu\mathrm{m}$ ($\approx 0.3\nu/u_\tau$).

Shear Stress Estimation From Tracks

In general, the viscous skin friction is related to the stream- and spanwise characteristics of the wall shear stress (WSS) vector $\vec{\tau}_w$. This quantity is closely linked to the flow dynamics in the viscous

sublayer near the no-slip wall and can be estimated using the tracer particle's velocity $\mathbf{u}$ and its distance from the wall y according to the following relation:

$$\vec{\tau}_w = \mu \left.\frac{\partial \mathbf{u}}{\partial y}\right|_{y=0} = \mu \lim_{y\to 0} \frac{\mathbf{u}(y)}{y} \approx \mu \frac{\mathbf{u}(\Delta y)}{\Delta y} \tag{1}$$

with x, y, z being the streamwise, wall-normal and spanwise coordinates and with μ the dynamic viscosity of the fluid. Since the gradient at the wall cannot be measured directly, the actual WSS can only be approximated using velocity data obtained at finite distance from the wall. In the results section, the superscript $(+)$ denotes viscous scaling where the length unit is defined as $l^* = \nu/u_\tau$, with ν being the kinematic viscosity and $u_\tau = \sqrt{\langle \tau_w \rangle / \rho}$ the friction velocity of the boundary layer flow.

The rate of change of the WSS was determined from the particle tracking data during weighted B-spline track fitting. Following an approach similar to that described in [17], the particle acceleration vector $\mathbf{a_p} = [a_{p,x}, a_{p,y}, a_{p,z}]$ is related to the rate of change of the WSS vector:

$$\frac{\partial}{\partial t}\left(\vec{\tau}_w\right) = \frac{\partial}{\partial t}\left(\mu \left.\frac{\partial \mathbf{u}}{\partial y}\right|_{y=0}\right) = \mu \left.\frac{\partial \mathbf{a}}{\partial y}\right|_{y=0} \approx \mu \frac{\mathbf{a_p}(\Delta y)}{\Delta y}. \tag{2}$$

In the following the symbol $\hat{a}$ refers to this quantity and in effect is the particle acceleration $a_{p,i}$ divided by the wall distance:

$$\hat{a}_i = \frac{\partial \tau_i}{\partial t} = \lim_{y\to 0} \frac{a_{p,i}}{y} \tag{3}$$

Uncertainty of shear stress

It is well known that estimating the WSS statistic from finite wall-normal distances introduces uncertainty, as the WSS is derived from the velocity gradient near the wall [2, 4, 17]. The two primary sources of uncertainty are the velocity error δu and the error in wall-normal distance detection, δy, both linked to particle position accuracy. The latter can be estimated from the 3d positions of particles adhering to the curved inner surface, provided low-frequency wall vibrations are filtered out. Additionally, the position accuracy can vary significantly with particle image intensity, as demonstrated by the root mean square (rms) of the positions of wall-attached particles of different brightness in Fig. 5.

For the present measurements, the uncertainty δu of individual velocity samples is estimated from the rms of the x-position of wall-attached particles, multiplied by the frame rate. The uncertainty δ_y is estimated from the rms of the y-position. The relative error ϵ_τ of the WSS can then be estimated

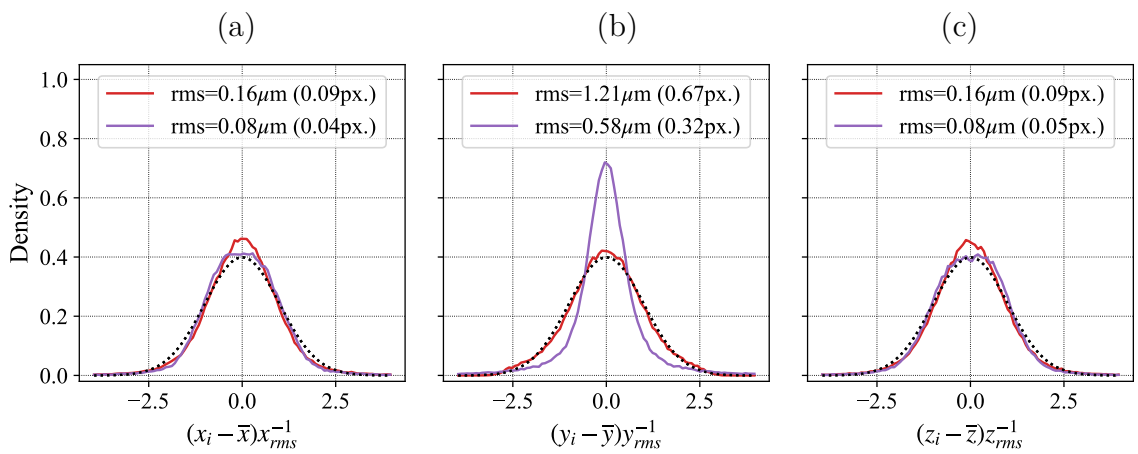

Figure 5. PDFs of 3d positions x (a), y (b), z (c) of particles of different intensity that stuck to the inner surface of the window at U_{cl}=8 m/s; The dotted line correspond to a Gaussian.

using classical error propagation laws:

$$\epsilon_{\tau_w}(y) = \frac{\delta\tau_w}{\tau_w} = \left[{\epsilon_u}^2 + {\epsilon_y}^2\right]^{0.5} \tag{4}$$

$$= \left[\left(\frac{\delta u}{u(y)}\right)^2 + \left(\frac{\delta y}{y}\right)^2\right]^{0.5} \tag{5}$$

Fig. 6 demonstrates the steep increase in the relative uncertainties toward the wall for particles with average intensity. For the present measurements and individual samples, the resulting relative errors in the WSS (Fig. 6(c)) range from 3% to 12% at the lower end of the relevant wall distance range ($y^+ = 0.5$) and decrease to 0.4%–1% near $y^+ = 4$. Following Benedict [3], the 95% confidence intervals for the mean and rms statistics can be estimated from single-sample uncertainty using:

$$\epsilon_{\langle x\rangle} = \frac{1.96}{\langle x\rangle}\sqrt{\frac{\delta_x^2}{N_{s,eff}}} \tag{6}$$

$$\epsilon_{x_{\mathrm{rms}}} = \frac{1.96}{\langle xx\rangle^{0.5}}\sqrt{\frac{\delta_x^2}{2N_{s,eff}}} \tag{7}$$

The number of uncorrelated samples $N_{s,eff} < N_s$ within the set N_s is estimated by considering the time duration of a sequence $t_t = N_t/f_s$ and the large eddy turnover time $t_b = R/U_{\mathrm{cl}}$, so that $N_{s,eff} = N_s \cdot t_b/t_t = N_s/N_{eff}$. As indicated by N_{eff} in Table 1, independent large eddies are captured at a rate of 140 to 379 per series. Since tracking particles requires uniform temporal sampling at relatively high frame rates and the number of sequences of representative length is limited by disk space, the relatively low N_{eff} are considered a necessary compromise.

When evaluating the 95% confidence limits for the mean WSS, the dashed lines in Fig. 6(c) indicate

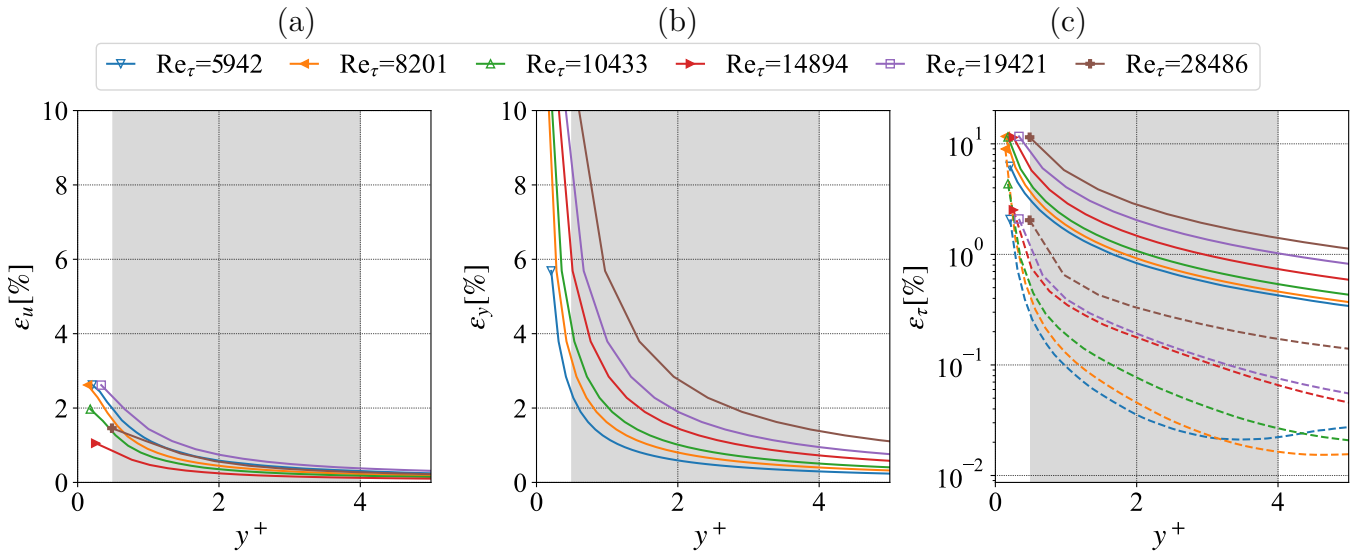

Figure 6. Relative error estimates: Velocity (a) wall-normal position (b) and WSS (c), solid lines: single sample, dashed lines correspond to 95% confidence based on Eq. (6) for bins of 8 µm; the shaded region correspond to the domain used for WSS evaluations at the highest Re.

a rapid decrease in random uncertainty from relative errors of $[0.2{-}2]\%$ at $y^+ = 0.5$ which drops below 1% approximately from $y^+ = 1$.

Results and Discussion

While the evaluation of the extensive data set is still ongoing, the following presents key insights into the recovered properties of the investigated turbulent pipe flow. The present application of MA-µPTV was primarily aimed at providing time-resolved measurements of the unsteady wall shear stress vector $\vec{\tau}_w$, along with its streamwise and spanwise components and their joint probability distributions – enabling access to friction Reynolds numbers previously unattainable by any other measurement technique.

Bin-averaged profiles of the mean and fluctuating near-wall velocities are presented in Fig. 7 and show very good agreement with DNS up to $y^+ \approx 5$, accurately capturing the viscous sublayer behavior, including the linear velocity profile and the characteristic scaling of the mean velocity gradient. This close match confirms the high spatial resolution and accuracy of the particle tracking velocimetry (PTV) setup in the near-wall region. As the wall distance increases beyond $y^+ \approx 5$, small deviations from DNS are observed, particularly in the streamwise velocity fluctuations and covariances. These deviations are likely attributable to incomplete particle tracking at larger wall distances. Due to the finite depth of field and the decreasing particle image intensity with increasing distance from the wall, longer particle tracks are no longer fully captured. This is corroborated by the decreasing bin density and track length observed in Fig. 3(a, b), which indicates a loss of

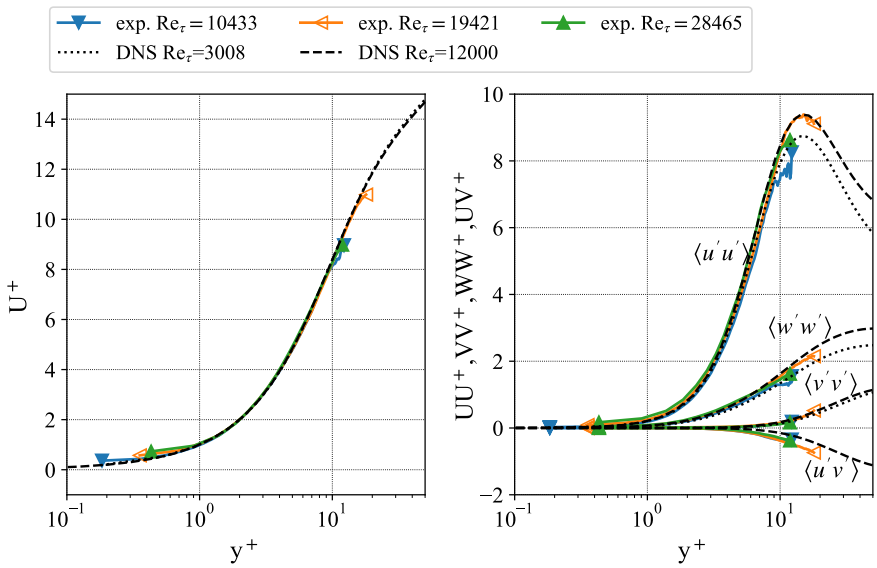

Figure 7. Mean and fluctuating velocities compared to DNS of turbulent pipe flow [1, 11]).

particle persistence in the measurement volume. As a result, the statistical sampling becomes less representative, leading to an underestimation of velocity fluctuations and their correlations. Notably, the covariance $u'v'$, shows a slight underprediction from $y^+ \gtrsim 5$, consistent with a reduction in track continuity and increased tracking ambiguity. This suggests that while the method captures the overall structure of the viscous layer, the statistical convergence in the buffer layer is limited by the physical constraints of the optical setup and the particle tracking algorithm.

Probability density distributions of the streamwise and spanwise components of the WSS vector are presented in Fig. 8. Although the distributions largely collapse, a slight Re dependence becomes apparent in the tails of τ_x'. Whether these deviations in the tails are truly Re dependent or due to measurement uncertainties is currently under investigation. However, while the overall shape of the probability density functions (PDFs) is invariant, the higher-order statistical moments — specifically skewness $S_{\tau x}$ and flatness $F_{\tau x}$, $F_{\tau z}$ (see table on top of Fig. 8) — confirm a slight dependence on Re. The skewness of the streamwise WSS component increases marginally with Re, while the flatness shows a stronger rise. This behavior is known from studies of flat plate TBL, which report a weak Reynolds number dependence of these moments [5, 17, 6]. In contrast, such dependence is less documented in turbulent pipe flows. The corresponding joint probability density functions (JPDFs) of the WSS components, shown in Fig. 9, confirm a universality across the investigated Reynolds number range. The shape of the JPDFs remains nearly invariant, indicating that the statistical structure of the wall shear stress fluctuations is governed by the same underlying dynamics regardless of Reynolds number. This universality has been previously observed in studies on flat plate TBL at lower friction Reynolds numbers [17], but this is the first experimental demonstration of such behavior at high Reynolds numbers in a turbulent pipe flow.

The focus is now on the root mean square (rms) of the WSS derived from near-wall particle tracks. Current literature on flat plate TBL provides a correlation for the Reynolds number dependence of

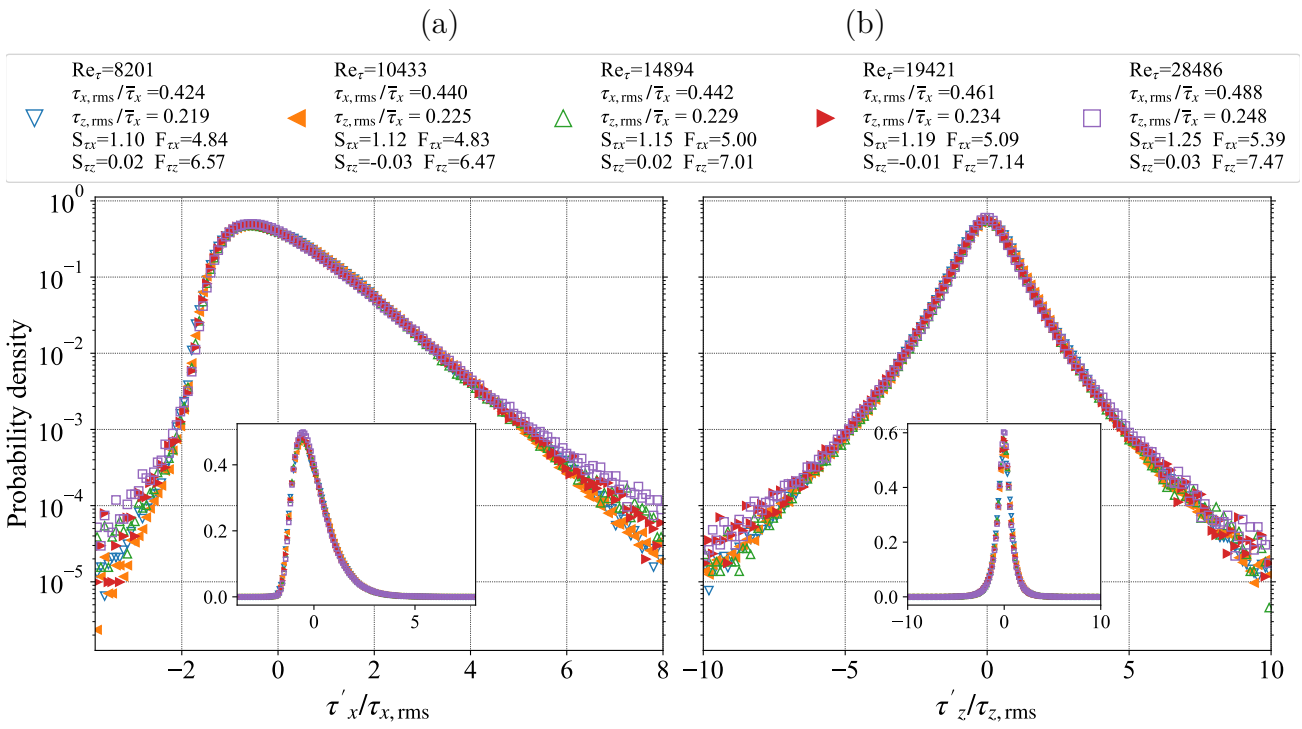

Figure 8. Streamwise (a) and spanwise (b) PDFs of the WSS vector evaluated from particle tracks in the viscous sublayer at $y^+ < 4$.

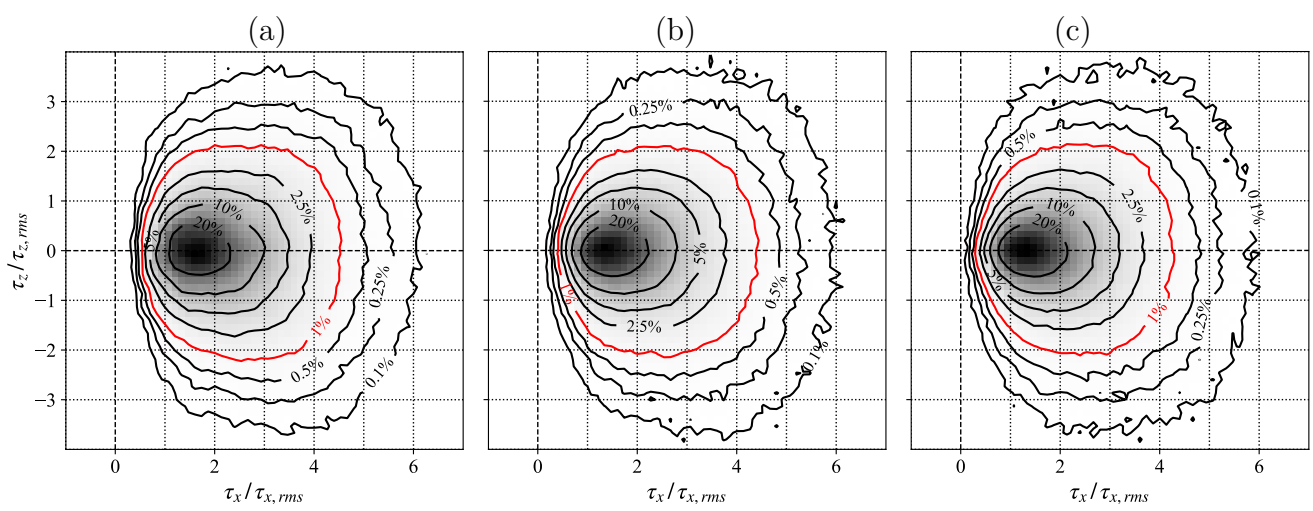

Figure 9. Joint PDF of the WSS vector evaluated from particle tracks in the viscous sublayer at $y^+ < 4$: (a) $\mathrm{Re}_\tau = 10433$ (b) $\mathrm{Re}_\tau = 19421$ (c) $\mathrm{Re}_\tau = 28486$.

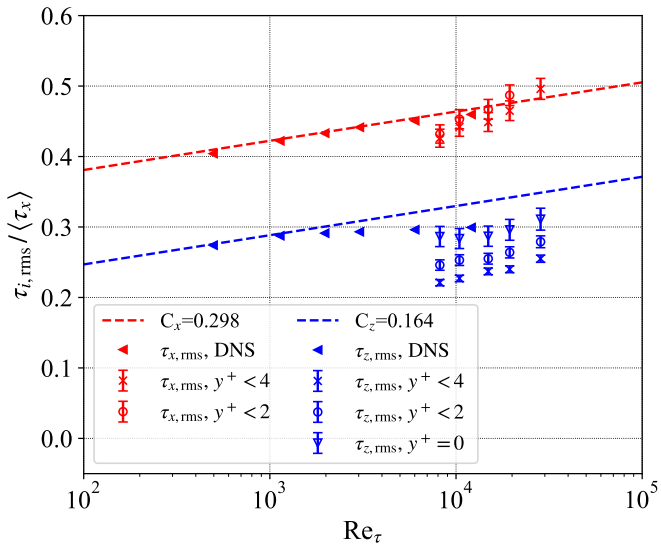

Figure 10. Root mean squared fluctuations of WSS components determined from particle tracks at $y^+ < 4$ (×, ×), at $y^+ < 2$ (○, ○) and extrapolated at the wall (▽); DNS of a pipe flow from [11]; dashed lines correspond to Eq. 8 with different offsets $C_x = 0.298$ [9] and $C_z = 0.164$ [5].

the rms of the WSS components of the form

$$\frac{\tau_{i,\mathrm{rms}}}{\langle\tau_x\rangle} = C_i + 0.018\, ln(\mathrm{Re}_\tau) \tag{8}$$

where $C_x = 0.298$ is proposed by [9] for streamwise fluctuations, and [5] proposed the same logarithmic dependence with $C_z = 0.164$ for spanwise fluctuations. These correlations are based on experimental and numerical data and have been confirmed by DNS of a flat plate TBL for Re_τ up to 2000 [12].

When comparing the present data with the correlation for the streamwise $\tau_{x,\mathrm{rms}}$ (see Fig. 10), good agreement is observed within measurement uncertainty for all but the two lowest Re, provided that fluctuation estimates are based on tracks within $y^+ < 2$. At the highest Re, however, the rms values tend to be overestimated, likely due to insufficient tracking accuracy. With regard to deviations at the lower Re one reason could be an insufficient number of independent samples with respect to the time scale of the largest eddies (see N_{eff}in Table 1).

Although the same logarithmic dependence is confirmed, values of $\tau_{z,\mathrm{rms}}$ obtained from particle tracks at $y^+ < 4$ and $y^+ < 2$ suggest a significantly lower offset C_z than the correlation proposed by [5] (see Fig. 10). Moreover, values derived from tracks closest to the wall exhibit less underestimation of the correlation, indicating a reduced deviation in the innermost wall-adjacent region from the reference model. The reason for this underestimation may lie in the fact that spanwise fluctuations increase more rapidly near the wall compared to streamwise fluctuations – similar to the behavior known for a flat plate TBL. For this reason, $\tau_{z,\mathrm{rms}}$ at $y^+ = 0$ was also extrapolated from bin-averaged profiles of the WSS estimates, using an approach similar to that described by [6]. The corresponding profiles are shown in Fig. 11, where the extrapolation is based on a weighted second-order polynomial fitting scheme. The weights are determined from the uncertainty estimated via Eq. 7. Returning to Fig. 10, extrapolated values at $y^+ = 0$ still exhibit a significant

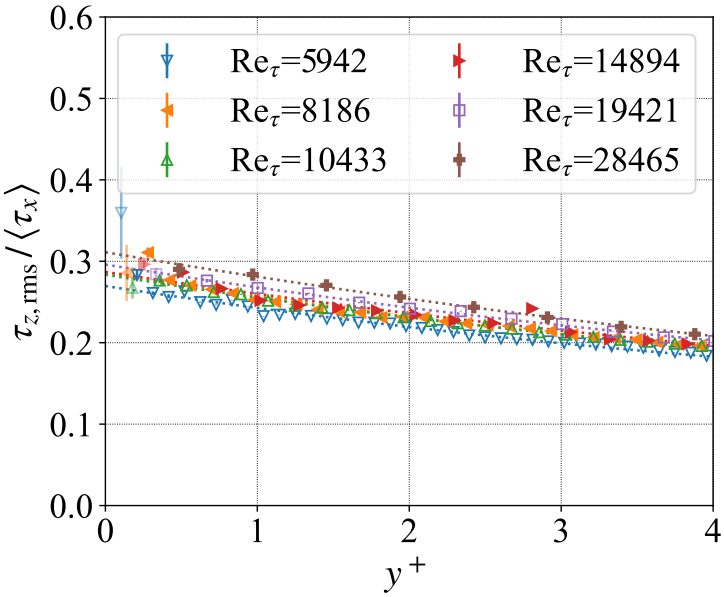

Figure 11. Extrapolation of spanwise WSS fluctuations from profiles of WSS estimates using particle tracks in the viscous layer. The dotted lines correspond to the weighted 2nd order polynomial fit for estimating the values at the wall.

underestimation relative to the correlations for a flat plate TBL. However, there is no clear explanation for the deviation when accounting for experimental uncertainty. In contrast, compared to spanwise rms values from DNS of pipe flows by [11], good agreement within a 5% measurement uncertainty is found for wall-extrapolated quantities. The discrepancy to correlations that are based on flat plate boundary layers may arise from geometric confinement, wall curvature, and the absence of a free stream in pipe flows, which may suppress large-scale spanwise coherent structures.

Aside from velocity and wall-distance, the accelerations in the reconstructed particle tracks provide estimates of the time derivative of the WSS, for which PDFs are compiled in Fig. 12. The PDFs reveal strongly non-Gaussian statistics, characterized by long tails corresponding to high-acceleration events. This behavior is consistent with previous observations of particle acceleration in turbulent flows [7, 13]. The streamwise PDF exhibits a slight negative skewness, a feature also observed in experiments and DNS of near-wall particle accelerations in a fully developed channel flow at $\mathrm{Re}_\tau = 1440$ by [13] and in measurements of a flat plate TBL at Re_τ 563 to 935 by [17]. Present measurements indicate that both the overall shape of the PDFs and the higher order moments skewness $S_{\hat{a}x}$ and flatness $F_{\hat{a}x}$, $F_{\hat{a}z}$ are Reynolds number independent (see table at the top of Fig. 12). This Reynolds number invariance supports the hypothesis that the near-wall dynamics of wall shear stress rate of change are governed by local viscous scaling, rather than large-scale outer-layer structures. Much like the velocity data, the joint probability density functions (JPDFs) in Fig. 13 exhibit a nearly Reynolds number-independent distribution with a slight negative mean. When evaluating the JPDFs of the WSS rate of change from particle tracks at different finite wall distances (see Fig. 13), it was observed that the distribution becomes increasingly isotropic and less skewed, particularly near the wall.

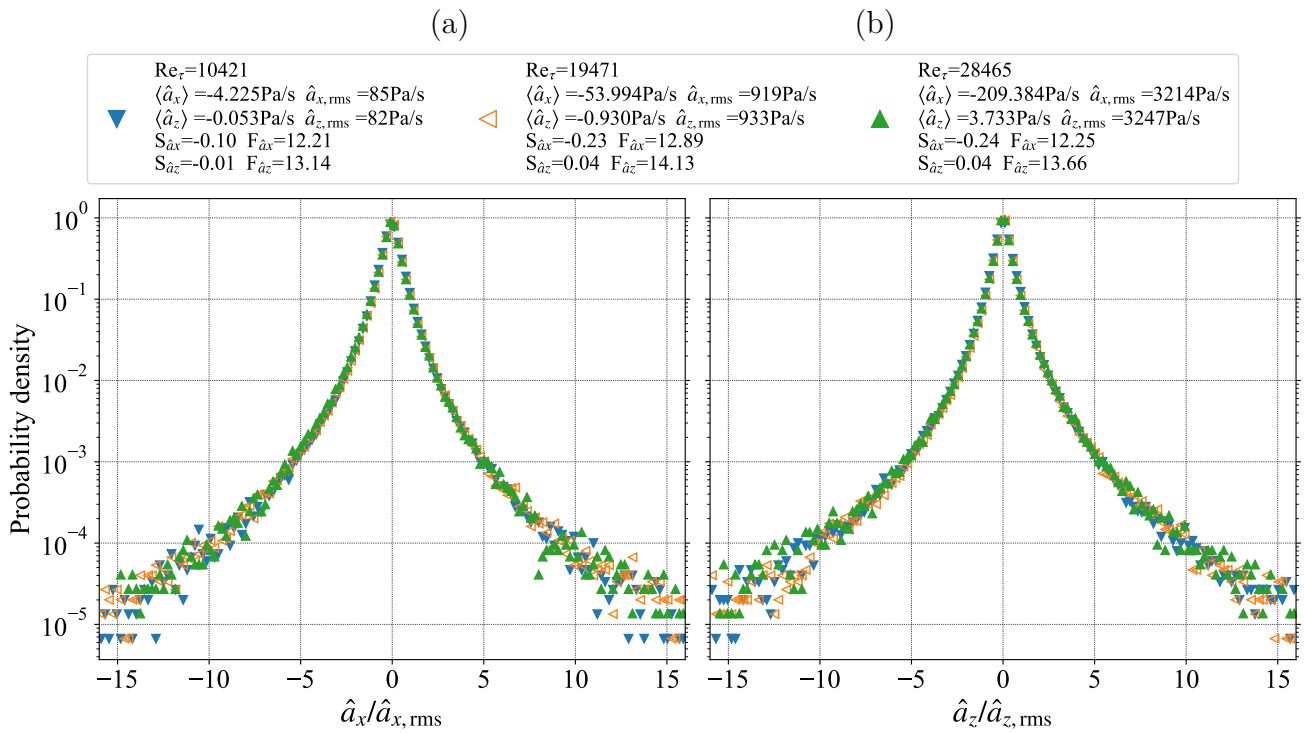

Figure 12. PDFs of WSS rate of change estimated from particle tracks in the viscous sublayer at $y^+ < 2$: (a) streamwise (b) spanwise component.

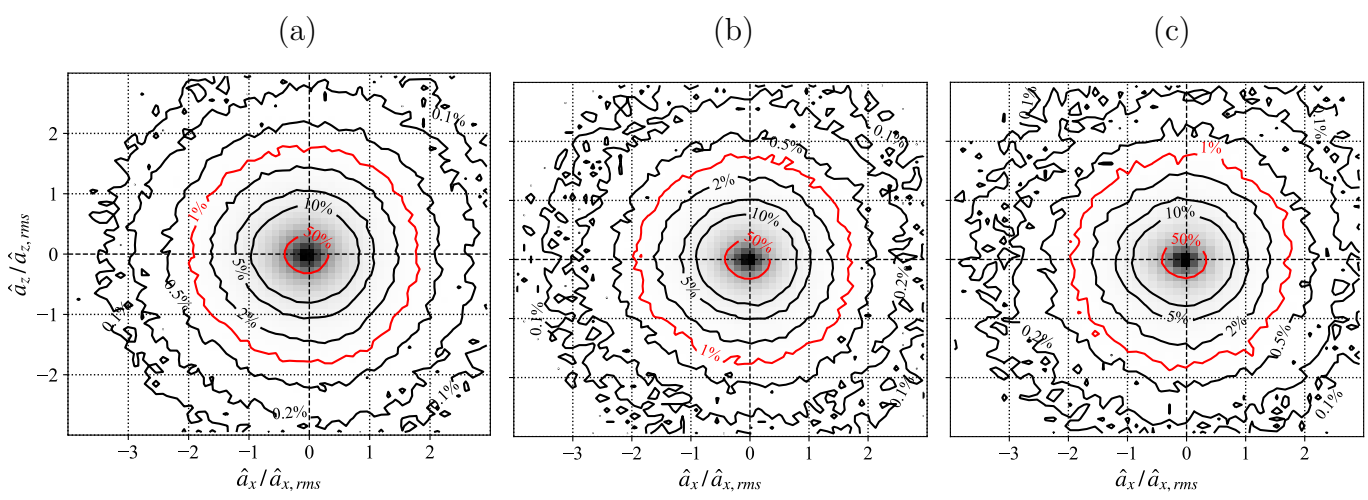

Figure 13. Joint PDF of WSS acceleration evaluated from particle tracks in the viscous sublayer at $y^+ < 4$: (a) $\mathrm{Re}_\tau = 10421$ (b) $\mathrm{Re}_\tau = 19421$ (c) $\mathrm{Re}_\tau = 28465$.

Conclusions

This study presents high-resolution, Lagrangian measurements of the wall shear stress (WSS) and its time derivative in a turbulent pipe boundary layer up to $\mathrm{Re}_\tau = 28400$ using single-camera, multi-aperture 3d-3c PTV. For velocity profiles, the method achieves a spatial resolution of $8\,\mu\mathrm{m}$, corresponding to approximately half of the smallest viscous length scale, enabling direct access to the viscous sublayer and capturing the near-wall turbulence with unprecedented fidelity. Excellent agreement with velocity profiles in the viscous sublayer from DNS confirms the robustness of the technique. Minor deviations at larger wall distances arise from tracking limitations due to finite depth of field and decreasing image intensity, not methodological flaws. The PDFs and JPDF of the unsteady WSS and its rate of change exhibit strong Reynolds number independence, supporting the self-similarity of near-wall dynamics governed by local viscous scaling. Minor variations in skewness and flatness of the WSS PDFs further support the idea that while the core statistical structure remains universal, subtle changes in intermittency emerge at higher Reynolds numbers. With regard to the rate of change of the streamwise and spanwise WSS the PDFs reveal strongly non-Gaussian statistics with long tails, consistent with intermittent turbulent dynamics. The spanwise component $\tau_{z,\mathrm{rms}}$ is significantly underestimated compared to correlations from flat plate TBL data, even after extrapolation to $y^+ = 0$. However, it shows good agreement with DNS data for pipe flows, which may be attributed to geometric confinement and the suppression of large-scale spanwise coherent structures in pipe flows. These results establish a new experimental benchmark for high-Re wall-bounded turbulence and provide a critical dataset for validating high-fidelity simulations and advancing turbulence modeling.

References

[1] Ahn, J., Lee, J.H., Lee, J., Kang, J.h., Sung, H.J.: Direct numerical simulation of a 30R long turbulent pipe flow at *Re* τ = 3008. Physics of Fluids **27**(6), 065,110 (2015). DOI: 10.1063/1.4922612

[2] Alfredsson, P.H., Örlü, R., Schlatter, P.: The viscous sublayer revisited–exploiting self-similarity to determine the wall position and friction velocity. Experiments in Fluids **51**(1), 271–280 (2011). DOI: 10.1007/s00348-011-1048-8

[3] Benedict, L.H., Gould, R.D.: Towards better uncertainty estimates for turbulence statistics. Experiments in Fluids **22**(2), 129–136 (1996). DOI: 10.1007/s003480050030

[4] Chen, Q., Duan, Y., Zhong, Q., Wang, Z., Huang, L.: On the method of determining instantaneous wall shear stress from near-wall velocity measurements in wall turbulence. Physics of Fluids **33**(12), 125,105 (2021). DOI: 10.1063/5.0068077

[5] Diaz-Daniel, C., Laizet, S., Vassilicos, J.C.: Wall shear stress fluctuations: Mixed scaling and their effects on velocity fluctuations in a turbulent boundary layer. Physics of Fluids **29**(5), 055,102 (2017). DOI: 10.1063/1.4984002

[6] Klinner, J., Willert, C.E.: Measurements of the unsteady wall shear stress vector using multi-aperture defocusing microscopic particle tracking velocimetry. Experimental Thermal and Fluid Science **163**, 111,395 (2025). DOI: 10.1016/j.expthermflusci.2024.111395. URL https://doi.org/10.1016/j.expthermflusci.2024.111395

[7] La Porta, A., Voth, G.A., Crawford, A.M., Alexander, J., Bodenschatz, E.: Fluid particle accelerations in fully developed turbulence. Nature **409**(6823), 1017–1019 (2001). DOI: 10.1038/35059027

[8] Malik, N.A., Dracos, T., Papantoniou, D.A.: Particle tracking velocimetry in three-dimensional flows. Experiments in Fluids **15**, 279–294 (1993). DOI: 10.1007/BF00223406

[9] Örlü, R., Schlatter, P.: On the fluctuating wall-shear stress in zero pressure-gradient turbulent boundary layer flows. Physics of Fluids **23**(2), 021,704 (2011). DOI: 10.1063/1.3555191

[10] Ouellette, N.T., Xu, H., Bodenschatz, E.: A quantitative study of three-dimensional Lagrangian particle tracking algorithms. Experiments in Fluids **40**(2), 301–313 (2006). DOI: 10.1007/s00348-005-0068-7

[11] Pirozzoli, S.: On the streamwise velocity variance in the near-wall region of turbulent flows. J. Fluid Mech. **989**, A5 (2024). DOI: 10.1017/jfm.2024.467

[12] Simens, M.P., Jiménez, J., Hoyas, S., Mizuno, Y.: A high-resolution code for turbulent boundary layers. Journal of Computational Physics **228**(11), 4218–4231 (2009). DOI: 10.1016/j.jcp.2009.02.031

[13] Stelzenmuller, N., Polanco, J.I., Vignal, L., Vinkovic, I., Mordant, N.: Lagrangian acceleration statistics in a turbulent channel flow. Physical Review Fluids **2**(5), 054,602 (2017). DOI: 10.1103/PhysRevFluids.2.054602

[14] Talamelli, A., Persiani, F., Fransson, J., Alfredsson, P.H., Johansson, A., Nagib, H., Rüdi, J.D., Sreenivasan, K., Monkewitz, P.: CICLoPE — a response to the need for high Reynolds number experiments. Fluid Dynamics Research **41**(2), 021,407 (2009). DOI: 10.1088/0169-5983/41/2/021407. URL https://dx.doi.org/10.1088/0169-5983/41/2/021407

[15] Willert, C., Gharib, M.: Three-dimensional particle imaging with a single camera. Experiments in Fluids **12**(6), 353–358 (1992). DOI: 10.1007/BF00193880

[16] Willert, C., Soria, J., Stanislas, M., Klinner, J., Amili, O., Eisfelder, M., Cuvier, C., Bellani, G., Fiorini, T., Talamelli, A.: Near-wall statistics of a turbulent pipe flow at shear Reynolds numbers up to 40 000. J. Fluid Mech. **826** (2017). DOI: 10.1017/jfm.2017.498. URL http://dx.doi.org/10.1017/jfm.2017.498

[17] Willert, C.E., Klinner, J.: Dynamic wall shear stress measurement using event-based 3d particle tracking. Experiments in Fluids **66**(2), 32 (2025). DOI: 10.1007/s00348-024-03946-2